Journal of
Materials Chemistry A

ROYAL SOCIETY
OF CHEMISTRY

PAPER

View Article Online
View Journal

Check for updates

Cite this: DOI: 10.1039/d6ta00420b

Revisiting MnP_4 as a negative electrode for Li-ion batteries: mechanism and performance

Julien Fullenwarth,[a] Bernard Fraisse,[a] Nicolas Dupré,[b] Lorenzo Stievano[ac] and Laure Monconduit*[ac]

Received 15th January 2026
Accepted 3rd March 2026

DOI: 10.1039/d6ta00420b

rsc.li/materials-a

MnP_4 has already been identified as a promising negative electrode for Li-ion batteries. Despite its interesting theoretical capacity, well above that of graphite, this material was not studied further due to its poor cyclability. MnP_4 was here prepared by ball milling and used as an active negative electrode material in optimised electrode formulation. This ball milled MnP_4 optimised electrode shows improving cycling performance, with a stable specific capacity of 600 mAh g^{-1} over 60 cycles. The combination of *operando* X-ray diffraction, Mn K-edge X-ray absorption spectroscopy, and ^{31}P and ^{7}Li NMR analyses reveals a two-step reversible mechanism: Li insertion in MnP_4 forming amorphous "Li_xMnP_4" which is converted into Li_3P and Mn metal at low potential. Unlike in previous studies related to MnP_4, the MnP_4 CMC-based electrode shows neither crystalline Li_7MnP_4 formation at mid discharge, nor MnP_4 reformation upon charge. This modified reaction pathway appears to be beneficial for long-term capacity retention.

1 Introduction

While the development of post-Li-ion batteries attracts growing attention, the development of alternative negative electrode materials combining high capacity and low operating potential remains essential to further boost the energy density of Li-ion batteries (LIBs). Transition metal phosphides (MP_x, where M is a transition metal) emerged nearly two decades ago as possible negative electrodes for LIBs and, more recently, for Na-ion batteries. These compounds are cost-effective and easily synthesized, and exhibit remarkable versatility and electrochemical performance.

Depending on their stoichiometry, the electronic properties of MP_x materials range from metallic to semiconducting. They also exhibit a wide range of intermediate stoichiometries, as exemplified by the Ni–P system,[1] including Ni-rich phosphides (Ni_3P, Ni_5P_2, $Ni_{12}P_5$, Ni_2P, and Ni_5P_4), mono-phosphide (NiP), and P-rich phosphides (NiP_2 and NiP_3).[2,3] Metal-rich MP_x, such as Mo_3P and Co_2P, are characterized by electron delocalization, leading to high electrical conductivity, advantageous for high rate cycling in batteries.[4–6] In contrast, P-rich MPs, such as MnP_4, FeP_4,[7] and CoP_4, exhibit a semi-metallic or semiconducting behavior depending on their local arrangements of MP_6 octahedra and the corresponding electronic structures.[8] This compositional and electronic diversity positions transition metal phosphides as key materials in energy storage research.

Lithiated MP_x are characterized by cubic close-packed phosphorus frameworks containing isolated metal-phosphorus tetrahedra, with lithium ions occupying both tetrahedral and octahedral sites. These structural features make this class of compounds particularly suitable for exploring various structure–property relationships and ion transport properties.[9]

Among them, MnP_4 can be considered as particularly attractive as a negative electrode for LIBs, thanks to its high theoretical capacity (1800 mA g^{-1}). Earlier studies suggested a mechanism based on the formation of Li_7MnP_4 followed by conversion into Mn and Li_3P.[23] However, in spite of its interesting capacity, MnP_4 showed poor cycling performance, likely due to the lack of appropriate electrode formulation in early investigations. Considering the significant advances achieved in electrode formulations over the past ten years, particularly for conversion electrode materials, MnP_4 deserves to be revisited under optimised conditions.

In the present work, MnP_4 was easily synthesised by reactive ball milling and evaluated as a negative electrode for LIBs using an optimized formulation. The material exhibits excellent capacity retention and rate capability, with minimal fading, even at high cycling rates. The electrochemical mechanism was elucidated within two potential windows by combining *operando* X-ray diffraction (XRD) with *operando* X-ray absorption spectroscopy (XAS), and both ^{31}P and ^{7}Li NMR spectroscopy.

2 Experimental section

2.1. Synthesis

1 g of MnP_4 was synthesized by ball milling as described in a previous paper.[10] Stoichiometric amounts of manganese metal

---

[a] *ICGM, Univ. Montpellier, CNRS, ENSCM, 34095 Montpellier Cedex 5, France. E-mail: laure.monconduit@umontpellier.fr*

[b] *Institut des Matériaux Jean Rouxel (IMN), CNRS UMR 6502, Université de Nantes, 44322 Cedex 3 Nantes, France*

[c] *Réseau sur le Stockage Electrochimique de L'Energie (RS2E), FR CNRS 3459, France*

(Mn Alfa Aesar, 325 mesh, 99.3%) and red phosphorus (P Alfa Aesar, 100 mesh, 99%) were placed in a 45 mL stainless steel jar with 6 balls of 10 mm diameter (4 g each ball), corresponding to a powder-to-ball ratio of 1 : 24. A Fritsch premium pulverisette 7 was used for 150 cycles (15 minutes milling + 10 minutes rest).

2.2. X-ray diffraction (XRD)

The XRD pattern of as-synthezised pristine MnP_4 was recorded on a Panalitical Empyrean diffractometer equipped with Cu Kα radiation in the Bragg–Brentano configuration.

Ex situ and *in situ* XRD measurements were carried out using a Leriche-type electrochemical cell equipped with a 250 µm-thick beryllium window in reflection mode.[11]

2.3. X-ray absorption spectroscopy (XAS)

In situ Mn K-edge XAS (6539 keV) measurements were carried out in transmission mode at the ROCK beamline[12] of synchrotron SOLEIL (France). A Si (111) channel-cut quick-XAS monochromator was used. The X-ray beam intensity was measured by using three consecutive ionisation detectors. Two *in situ* electrochemical cells,[11] assembled under the same conditions used in *in situ* XRD measurements, were placed between the first and the second ionisation chambers on a sample holder allowing rapid switching between them, so that their reaction could be followed simultaneously. The cells were cycled for over 1.5 cycles (lithiation/delithiation/lithiation) in different potential ranges (between 0.4 and 1.5 V, and between 0.01 and 1.5 V, respectively). 149 and 161 successive spectra were obtained for the two cells, respectively, by averaging out spectra collected at a rate of 2 Hz over periods of 10 minutes. The corresponding electrochemical curves are shown in the SI section. The whole *operando* XAS dataset was globally analysed using a chemometric approach including Principal Component Analysis (PCA) and Multivariate Curve Resolution-Alternating Least Squares (MCR-ALS).[13–15] The application of such a data analysis approach to the study of the electrochemical mechanism of battery materials has been described in full detail elsewhere.[15–17] The reconstructed pure spectral components as well as the spectrum of pristine Mn were fitted using the Demeter software package.[18] EXAFS amplitudes and phase-shifts were calculated by FEFF7 starting from the lattice parameters of Mn, MnP_2 and MnP_4. Interatomic distances (R) and the Debye–Waller factors (σ^2) were calculated for all paths included in the fits.

2.4. Magic angle spinning nuclear magnetic resonance (MAS NMR)

^7Li and ^{31}P MAS NMR experiments were carried out at room temperature on a Bruker Avance-500 spectrometer ($B_0 = 11.75$ T, Larmor frequency $\nu_0(^7Li) = 194$ MHz and $\nu_0(^{31}P) = 202.45$ MHz). MAS spectra were obtained by using a Bruker MAS probe with a cylindrical 2.5 mm o.d. zirconia rotor. Spinning frequencies up to 25 and 30 kHz were utilized. ^7Li NMR spectra were acquired using a single sequence with a $\pi/2$ pulse of 1 µs. ^{31}P NMR spectra were acquired by making use of a single $\pi/2$ pulse sequence of 4 µs. Recycle delays of 5 s were determined to ensure quantitative measurements for both ^7Li and ^{31}P. The isotropic shifts, reported in parts per million, are relative to external 1 M solutions of LiCl and H_3PO_4 in water set at 0 ppm. NMR integrated intensities were determined by spectral simulation using the Dmfit software.[19]

2.5. Electrode formulation

For electrode formulations, Timcal C65 carbon black and Showa Denko Carbon Fiber VGCF-H were used as conductive additives, and carboxymethyl cellulose (CMC) (DS = 0.7, M_w = 250 000 Aldrich) was used as a binder. 63 wt% MnP_4, 21 wt% conductive carbon additives and 16 wt% CMC binder were introduced in a 12 mL agate vial and ground for 1.5 h with a Fritsch Pulverisette 7 planetary mill. The slurry, obtained by adding deionized water (0.6 mL for 140 mg active material) to the mixture, was tape cast using a manual 150 µm doctor blade on 20 µm thick copper foil, then dried for 12 h at room temperature and then for 2 h at 100 °C under vacuum.

Electrodes with a higher tap density were necessary for the XAS experiments in order to optimize sample absorption and edge-jump (around 3–4 mg cm^{-2}). For such electrodes, 74 wt% MnP_4, 13 wt% conductive carbon additives and 13 wt% CMC binder were introduced into a 12 mL agate vial and ground for 1.5 h with a Fritsch Pulverisette 7 planetary mill. Deionized water (1.1 mL for 300 mg active material) was added to the electrode composite recovered after ball milling. The so-obtained slurry was tape cast with a manual 200 µm doctor blade onto a mylar foil and dried for 12 h at room temperature. Self-supported electrode films were punched from the cast film and dried under vacuum between two glass plates for 2 h at 100 °C.

2.6. Electrochemical characterisation

Galvanostatic lithium insertion/extraction tests in MnP_4 were carried out in two-electrode half-cell configuration *vs.* Li metal (Sigma-Aldrich 99.9% ribbon) with a 1 M $LiPF_6$ in EC: PC: 3DMC electrolyte, containing 1% VC and 5% FEC. CR2032 coin cells were assembled in an argon filled glove box using an MTI MSK-160 crimping machine.

3 Results

The conventional synthesis of MnP_4 typically requires high-pressure conditions, or a tin-flux route.[20] Here, MnP_4 was synthesized for the first time by ball milling, yielding poorly crystalline MnP_4 with particle sizes ranging from 0.5 to 10 µm, composed of agglomerates of smaller primary crystallites (0.1–0.5 µm, see Fig. SI 1 for details). The XRD patterns of the ball milled powder, shown in Fig. SI 2, was refined in triclinic space group P-1 with cell parameters $a = 16.320(1)$ Å, $b = 5.8499(5)$ Å, $c = 5.1053(6)$ Å, $\alpha = 115.659(8)°$, $\beta = 95.138(1)°$, and $\gamma = 89.214(5)°$, in good agreement with ICSD 16416.

The structure of MnP_4 is described by tetramers of edge-shared octahedra linked to each other by P–P bridges to form a two-dimensional network of interconnected zigzag chains, in the (b,c) plane (Fig. SI 2). This tetramer packing forms a layered structure with short interlayer P–P distances (2.27 Å), as

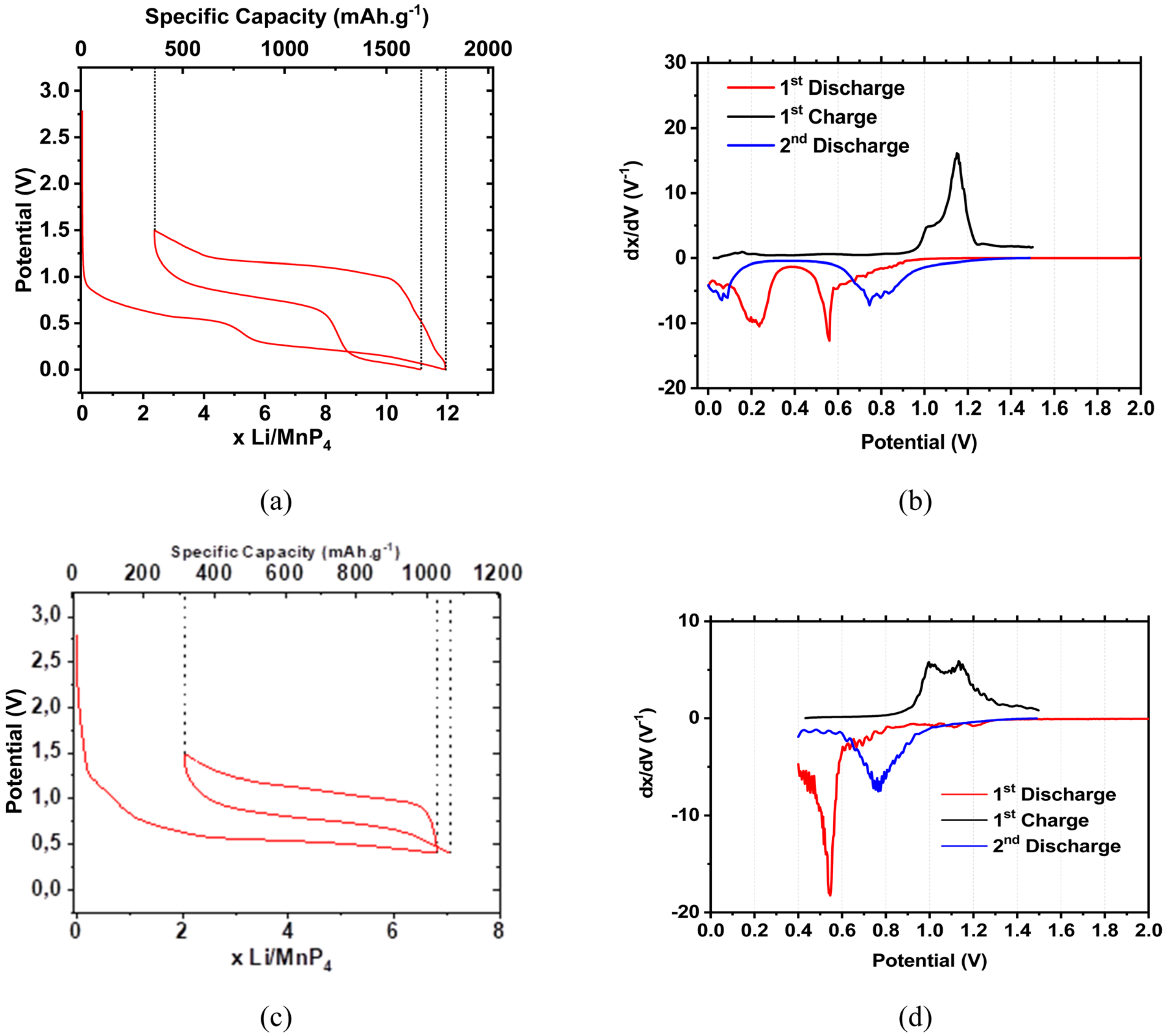

Fig. 1 Galvanostatic curves at C/2 and associated derivative curve of MnP_4 *vs.* Li cells in the 0–1.5 V potential window (a and b) and in the limited 0.4–1.5 V potential window (c and d).

extensively discussed in previous studies on ternary transition metal pnictides.[21,22]

The galvanostatic discharge of MnP_4 is shown in the 0–1.5 V and 0.4–1.5 V potential windows (Fig. 1(a) and c respectively). In the 0–1.5 V window, a sloping potential curve is observed from 1 to 0.3 V, corresponding to the insertion of 5–7 mol of Li per mol of MnP_4, followed by a second step corresponding to the reaction of more than 5 mol of Li. For the second discharge, the first process occurs at higher potential in both potential windows, and in the full potential window the second process is limited in the amount of inserted Li (<2 Li). An additional cut-off cycling is shown in Fig. SI 3, in the 0.5–1.5 V window, confirming the same electrochemical signatures.

For both potential windows, the derivative curves of the first discharge (Fig. 1(b–d)) show a main peak at 0.55 V, while a second broad peak appears at 0.2 V for the full potential window. During the first charge two oxidative peaks appear at 1 and 1.15 V, in both cases.

The second discharge curve is strongly modified, with a derivative peak now centred at 0.8 V, and a second one at 0.2 V in the full electrochemical window. The performance of MnP_4 under both cycling conditions is summarized in Table 1.

The first charge capacities obviously depend on the applied potential limits and are 1432, 716 and 397 mAh g^{-1} for the 0–1.5 V, 0.4–1.5 V, and 0.55–1.5 V potential windows, respectively. In the three situations, low initial coulombic efficiencies (ICEs) are measured: 80, 70.2 and 73.2% for the 0–1.5 V, 0.4–1.5 V, and 0.55–1.5 V potential windows (*cf.* Fig. SI 3), likely due to the electrolyte degradation leading to the formation of a solid electrolyte interphase (SEI), as well as the irreversible Li^+ insertion/adsorption in carbon additives.

It is worth noting that this solid electrolyte interphase (SEI) forms on all electrode components. To determine the impact of carbon additives, we performed an electrochemical measurement on a CMC-based electrode containing only C65 and VGCF (1 : 1). As illustrated in Fig. SI 4, the initial coulombic efficiency

Table 1 Electrochemical performance of MnP_4 electrodes at C/2, dependence on the potential window

Potential window	Initial Coulombic efficiency (ICE) %	1st discharge capacity (mAh g^{-1})	1st charge capacity (mAh g^{-1})	Charge capacity (mAh g^{-1}) [cycle *n*°]	Coulombic efficiency (CE) [cycle *n*°]
[0–1.5 V]	80%	1788	1432	754 [15]	99.9% [15]
[0.4–1.5 V]	70.2%	1020	716	734[15] 621 [55]	99.7% [15] 100.4% [55]
[0.55–1.5 V]	73.2%	542	397	480 [15] 503 [55]	100% [15] 99.7% [55]

(ICE) of this electrode is approximately 43% (147% during the first discharge and 63% during the first charge). This very low ICE, comparable to that of the MnP4 electrode, will justify future optimization by modifying these carbon additives.

The capacity retention measured at a C/2 rate in the three potential windows is given in Fig. 2 (1C is defined as the reaction of 1 mol of Li per mol of MnP_4 per hour, *i.e.*, 200 mA g^{-1}).

Cycling in the 0–1.5 V potential window leads to rapid capacity fading. Contrarily, cycling in the windows with a higher low potential cut-off, where the low potential process is absent, retains 100% of the first charge capacity after 15 cycles and displays only low to negligible capacity fading upon prolonged cycling. After 50 cycles, a capacity of 621 mAh g^{-1} is still maintained in the 0.4–1.5 V potential window, which corresponds to 87% of the first charge. In the 0.55–1.5 V potential window (see complementary details in Fig. SI 10) the total initial charge capacity is maintained after 55 cycles, demonstrating the high efficiency of the MnP_4 electrode, and all the more so when the low potential process is avoided. The rate capability of the MnP_4/Li cell was tested in both full and limited 0.55–1.5 V potential windows with currents ranging from C/10 to 2C (Fig. SI 5). This shows a clear capacity decrease when the rate is increased. During the initial cycles, within moderate cycling rate operation, the increase in the rate to C/5 and C/2 has a limited impact on the delivered capacity, from 1100 to 900 and from 580 to 500 mAh g^{-1} in the full and limited potential windows, respectively. However, when further increasing the cycling rate to C and 2C, the system struggles to maintain its performance.

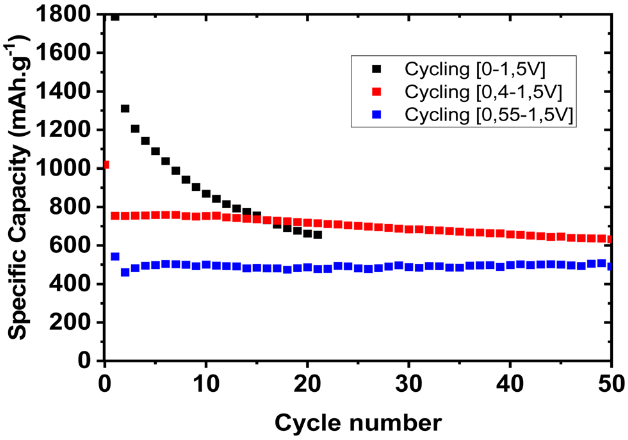

Fig. 2 Charge capacity retention measured at C/2 of the MnP_4/Li cell in the 0–1.5 V, 0.4–1.5 V and 0.55–1.5 V potential windows.

To gain insight about the two electrochemical processes identified from the derivative curves (Fig. 1 and 2), an *operando* XRD analysis was carried out on a MnP_4/Li cell in both 0–1.5 V and 0.4–1.5 V potential windows (Fig. 3 and 4). Despite the relatively poor quality of the XRD patterns due to the low crystallinity of the materials obtained by ball milling, several trends could be identified. During the first process, associated with the derivative peak at 0.5 V, the pristine MnP_4 pattern remains unchanged, and no additional peaks are detected. No trace of crystalline Li_7MnP_4 (fcc, $Fm\bar{3}m$, 00-014-0045, *cf.* Fig. SI 6) could be detected, as previously observed with MnP_4 obtained by high temperature synthesis.[23] Contrarily, during the second step, from 0.4 to 0 V, the two main Bragg peaks of MnP_4 at 32° and 33° strongly decrease in intensity, while simultaneously one new broad peak appears at around 27°. This peak could be assigned to hexagonal Li_3P ($P6_3$/mmc, 00-004-0525, *cf.* Fig. SI 6). It is notable that the second peak at around 26° could be mistaken for the peak of carbon fibers (*cf.* Fig. SI 7) preventing an unambiguous assignment. Interestingly, and in contrast with previous studies,[20,23] MnP_4 does not reappear at the end of the following charge, while only the carbon fiber peak can be clearly identified in the XRD pattern. *Operando* XRD analysis was also performed in the limited 0.4–1.5 V potential range (Fig. 4). In this case no modification of the XRD pattern is observed, suggesting that Li^+ insertion and deinsertion take place within the pseudo-layered structure of MnP_4 without significant structural modification.

To confirm the conclusions drawn from *operando* XRD, *ex situ* XRD measurements were also performed for selected samples cycled in both 0–1.5 V and 0.55–1.5 V potential windows (Fig. SI 8). For electrodes cycled in the full potential window, the disappearance of MnP_4 is confirmed at 0 V, as well as the formation of poorly crystalline Li_3P. At the end of charge, at 1.5 V, no signal is observed, except the signature of VGCF. In the 0.55–1.5 V potential window, on the other hand, no noticeable change is detected between the XRD pattern of the pristine electrode and of those discharged to 0.55 V or recharged to 1.5 V, confirming the possible topotactic Li insertion as suggested by *operando* XRD data.

A detailed ^{7}Li and ^{31}P MAS NMR analysis was carried out to further identify the lithiated phases and clarify the chronology of their formation, Fig. 5 displays the normalized ^{31}P MAS NMR spectra of as-synthesised MnP_4, as well as of the pristine MnP_4 electrode, containing 15 wt% of conductive carbon additives. While the signal-to-noise ratio of the spectrum of pure MnP_4 is sufficient to observe several resonances ascribed to the different

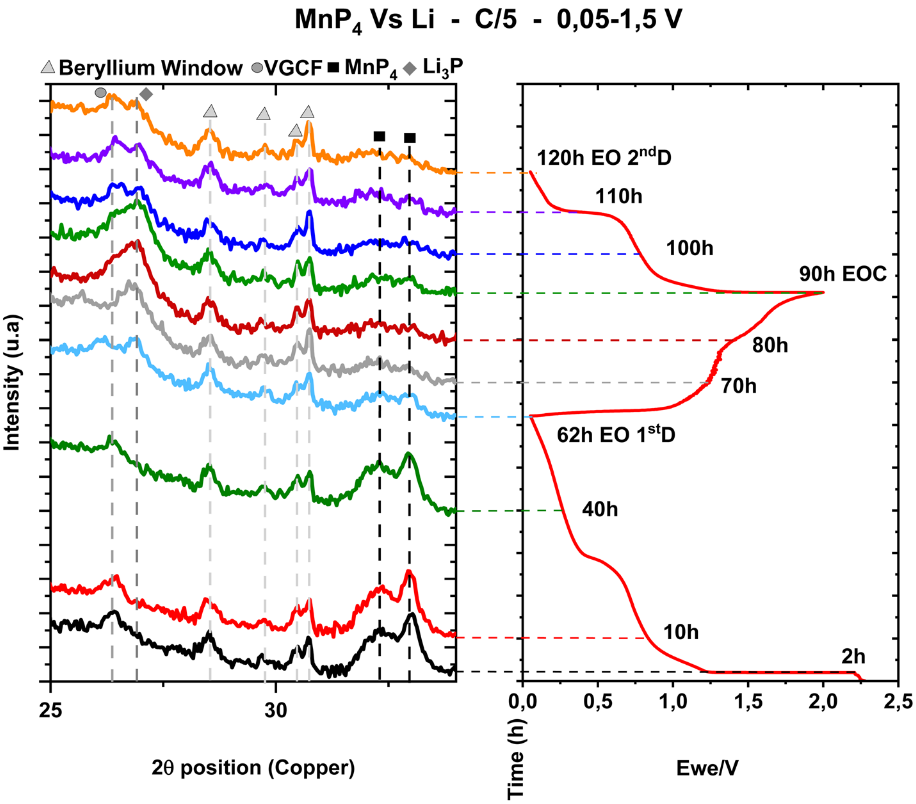

Fig. 3 *Operando* XRD pattern of the MnP_4/Li cell during the initial cycles at x (rate) in the [0–1.5 V] potential window and the associated galvanostatic curve.

local phosphorus environments in MnP_4, the spectrum of the electrode shows a much poorer signal-to-noise ratio even though thrice as many scans were acquired in this case. Normalized spectra of a pristine MnP_4 and a MnP_4 electrode are displayed in Fig. 9(a). The signal intensity decreases by approximatively 77.3% in the case of the electrode. As the presence of a conductive carbon additive is the sole difference between the two sample, we ascribe this signal loss to its presence. The conductive carbon, homogeneously distributed at the surface of the MnP_4 active material could lead to (i) an effect similar to a skin effect[24–28] and/or (ii) a probe detuning effect[29] and thus to RF pulse dissipation, reduced excitation and signal attenuation.

NMR experiments on the pristine material at various MAS speeds (Fig. SI 9) allowed the identification of 2 major isotropic resonances at 47 and 242 ppm, along with 2 additional weaker resonances at −35 and 170 ppm. All these signals are assigned to the different phosphorus environments in MnP_4. In addition, a minor sharp resonance at 15 ppm is attributed to a phosphate surface impurity, commonly observed in these materials. Although the weak resonances at 170 and -35 ppm are difficult to detect in the electrode spectrum, the main resonances at 47 and 242 ppm provide a clear signature of the presence of MnP_4 in the cycled electrodes (Fig. 5).

The relatively small chemical shifts suggest an overall diamagnetic behaviour, consistent with the previous work by Bekaert *et al.* on a series of metal phosphides. In particular, the chemical shift range measured for MnP_4 (−35 to 242 ppm) closely resembles that reported for diamagnetic FeP_4 (55 to 180 ppm).[30]

Fig. 6 displays the ^{31}P MAS NMR spectra of cycled electrodes, with those of the pristine electrode and as-synthesised MnP_4 reported as references. The same excitation dissipation problem is encountered in the case of the cycled electrodes, due to the presence of the conductive carbon additives. The ^{31}P MAS NMR spectra of the MnP_4 electrode discharged to 0 V (Fig. 6, green line) clearly shows that most of the initial MnP_4 has reacted, as none of the initial MnP_4 resonances can be observed. A sharp and intense signal at −270 ppm attributed to Li_3P is observed, in agreement with a previous observation by Marino *et al.*[31] The sharp resonance initially present at 15 ppm on the spectrum of the pristine material shifted to 10 ppm, suggesting that the surface phosphate impurity has also reacted during lithiation upon contact with the electrolyte or participating in the discharge process.

The spectrum obtained at the end of the following charge (Fig. 6, blue) does not display any evidence of Li_3P, indicating that Li_3P formed upon discharge to 0 V is reversibly oxidised. Nevertheless, the initial MnP_4 resonances do not reappear, suggesting that the manganese phosphide species forming upon charge are extremely disordered and quite different from the pristine material. Only an extremely broad signal can be seen between −50 and 200 ppm, indicating again that the phosphorus local environments are not well-defined after the removal of lithium.

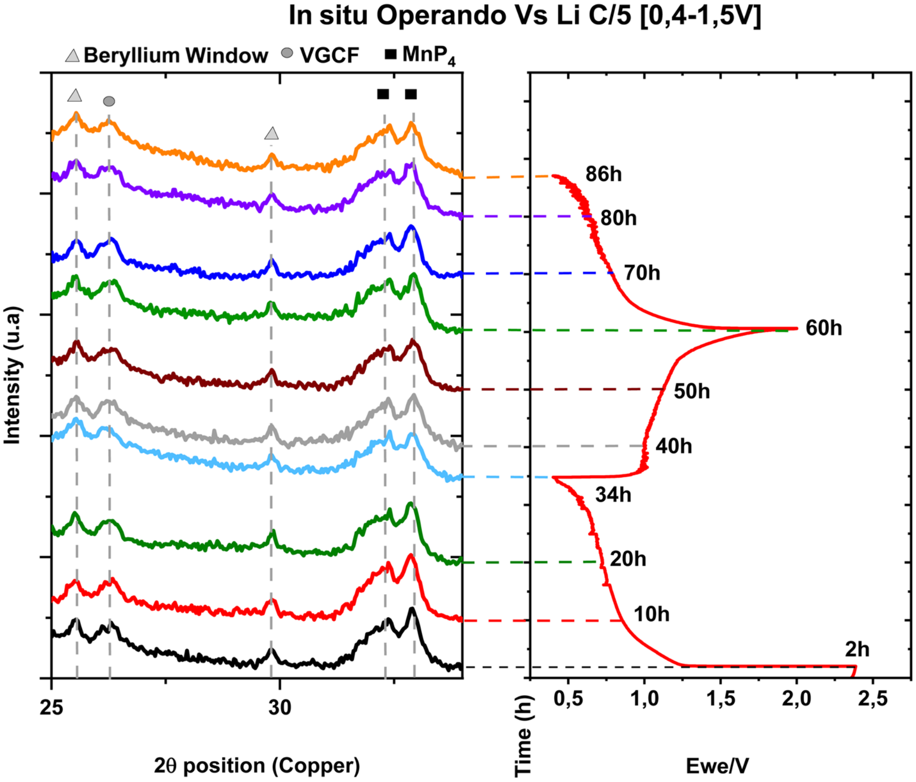

Fig. 4 *Operando* XRD pattern of the MnP_4/Li cell during the initial cycles at *x* (rate) in the [0.4–1.5 V] potential window and the associated galvanostatic curve.

The ^{31}P MAS NMR spectrum of the electrode stopped at 0.4 V (Fig. 6, black) appears quite different from that at 0 V. The typical resonances of pristine MnP_4 are clearly still visible, in agreement with XRD analyses. Nevertheless, a very broad signal appears near −270 ppm, possibly corresponding to phosphorus local environments close to Li_3P. While it is possible that local environments close to Li_3P are forming, this does not necessarily mean that crystalline Li_3P is already present, NMR being a local probe that will typically give information on the chemical vicinity within a few Angströms only. This suggests that either isolated and/or disordered phosphorus environments similar to (or close to) Li_3P start to form at 0.4 V but a lower potential is needed to fully achieve the formation of crystalline Li_3P, as detected by XRD. The sharp resonance at 10 ppm suggests that the surface phosphates have already reacted with the electrolyte. Resonances assigned to MnP_4 are also clearly visible in the ^{31}P MAS NMR spectrum after the subsequent charge back to 1.5 V (Fig. 6, purple) and seem to be more intense compared to in the spectrum at 0.4 V, consistent with the delithiation process to form MnP_4. Moreover, the broad signal at −270 ppm has disappeared, confirming that it is related to phosphorus local environments with lithium in its vicinity.

Fig. 7 displays the ^7Li MAS NMR spectra of the 4 cycled samples. All spectra show a single resonance close to 0 ppm. The ^7Li spectrum obtained at the end of discharge at 0 V is clearly more intense compared to that at 0.4 V, in agreement with the reaction with a higher amount of lithium ions. The two-step expected reaction ($MnP_4 + 7Li \rightarrow Li_7MnP_4$, followed by $Li_7MnP_4 + 5Li \rightarrow 4\ Li_3P + Mn$) would lead to a 7/12 (*e.g.*, 0.58) intensity ratio. In the present case, an intensity ratio of 0.48 is found. While the two values are close enough and the discrepancy could be ascribed to uncertainties in the ^7Li integrated

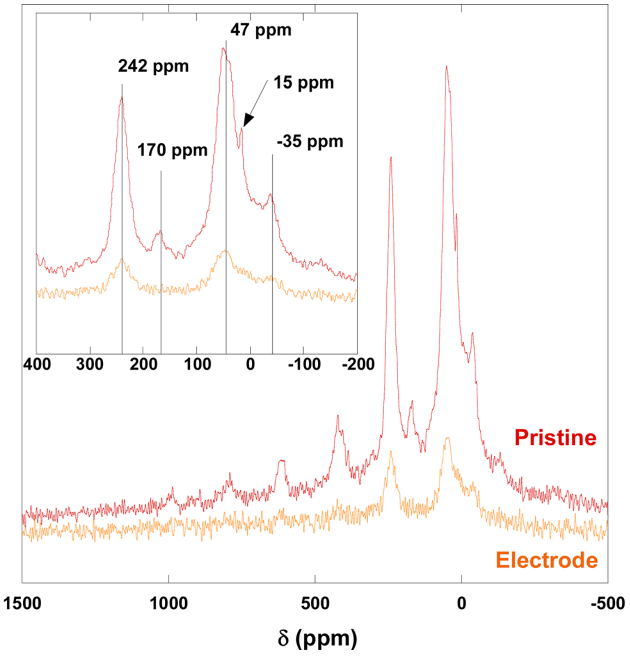

Fig. 5 Normalized ^{31}P MAS NMR spectra of MnP_4 as obtained from the synthesis (red) and the MnP_4 electrode prior to cycling (orange).

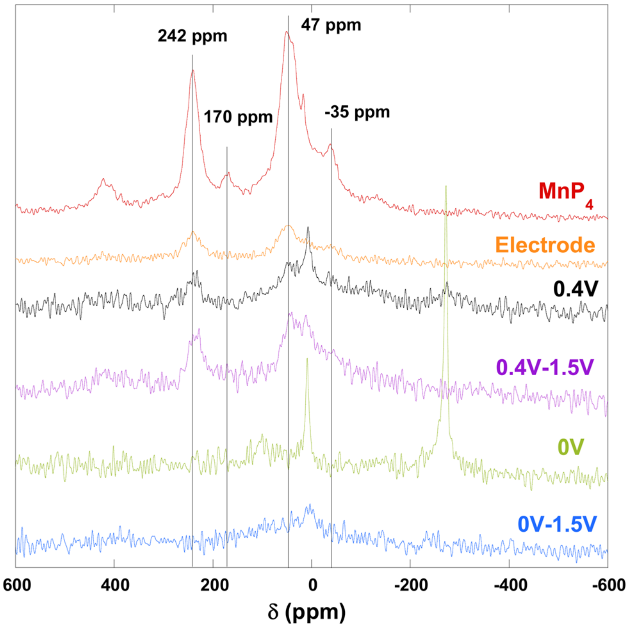

Fig. 6 ^{31}P MAS NMR spectra of (from top to bottom) MnP_4 (red), the MnP_4 uncycled electrode (orange), and MnP_4 electrodes discharged to 0.4 V (black), discharged to 0.4 V and charged to 1.5 V (purple), discharged to 0 V (green), discharged to 0 V and charged to 1.5 V (blue). The black lines indicate the initial ^{31}P MnP_4 resonances.

intensity connected to the formation of the SEI, NMR provides no clear evidence of the formation of Li_7MnP_4. The two spectra acquired at the end of charge (after discharge to 0 V and 0.4 V, respectively) display almost identical integrated intensities, suggesting that most of the SEI is already formed at 0.4 V.

Since the ^{7}Li MAS NMR spectrum of the electrode discharged to 0 V exhibits a slight shift with respect to that discharged at 0.4 V, spectra of the two discharged samples were acquired at 500 MHz to obtain a higher spectral resolution (Fig. 7, right). The ^{7}Li MAS NMR spectrum of the sample discharged to 0 V clearly shows two partially overlapping resonances, centred at −1 and 3 ppm. The resonance centred at −1 ppm, also present in the spectrum of the samples discharged at 0.4 V seems to contain both lithium in the SEI and lithium that has reacted with MnP_4 above 0.4 V. The second resonance is consistent with the chemical shift of Li_3P,[31] confirming its presence at the end of discharge at 0 V.

Further complementary information about the electrochemical mechanism in MnP_4 was gathered by XAS in two parallel experiments. The first cell (hereafter called cell XAS-INS, see Fig. SI 12) was cycled in the potential range of 0.4–1.5 V in order to verify the electrochemical mechanism in the expected insertion region of MnP_4, whereas a second cell (hereafter called cell XAS-CON) was cycled in the range of 0.01–1.5 V (SI 15) to probe the full conversion reaction domain of the material.

For the first experiment, the 149 spectra collected along the whole first discharge are shown in Fig. 8. A chemometric approach was used in order to extract the maximum information from this whole series of *operando* full XAS spectra (including both the near-edge (XANES) and the extended fine structure (EXAFS) portions) collected during the first 1.5 cycles.

The results of PCA (Fig. SI 13) indicate the presence of 3 to 5 dominant principal components expressing more than 99.9% of the variance of the whole dataset. The inspection of their shape and of the evolution of their scores confirm this assumption, with the subsequent principal components showing mostly noise in the EXAFS region of the spectra. Five

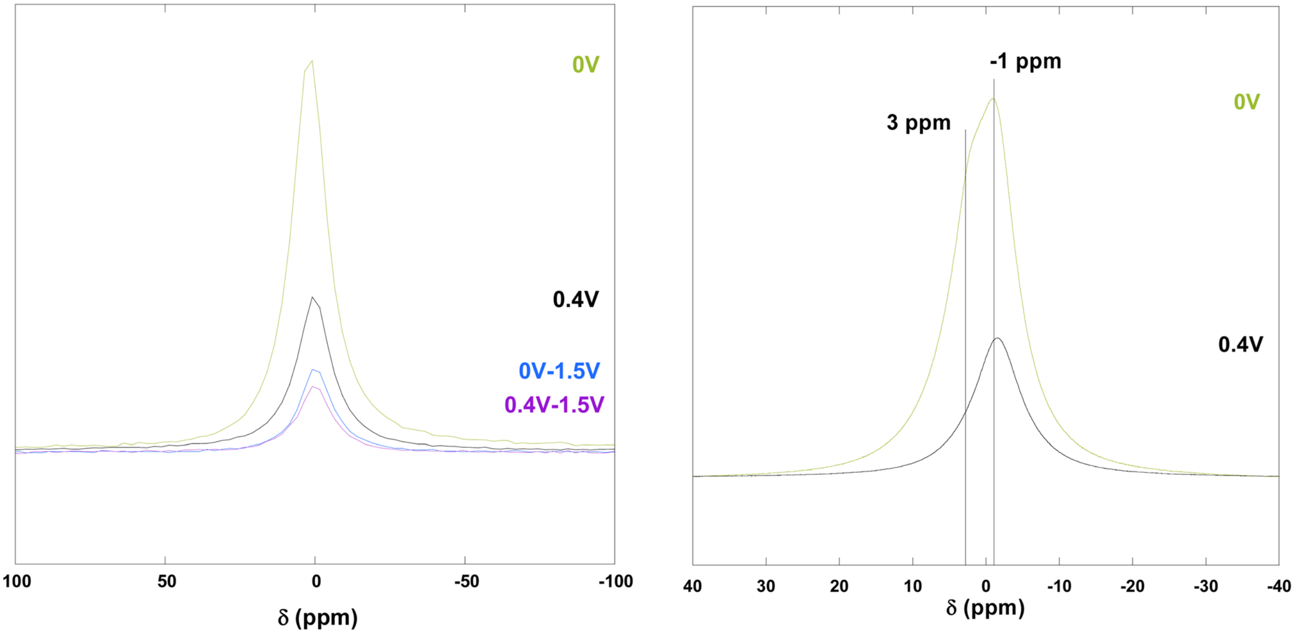

Fig. 7 (left) Normalized ^{7}Li MAS NMR spectra acquired at 200 MHz for MnP_4 electrodes discharged to 0.4 V (black), discharged to 0.4 V and charged to 1.5 V (purple), and discharged to 0 V (green), discharged to 0 V and charged to 1.5 V (blue). (right) Normalized ^{7}Li MAS NMR spectra acquired at 500 MHz for MnP_4 electrodes discharged to 0.4 V (black), and discharged to 0 V (green).

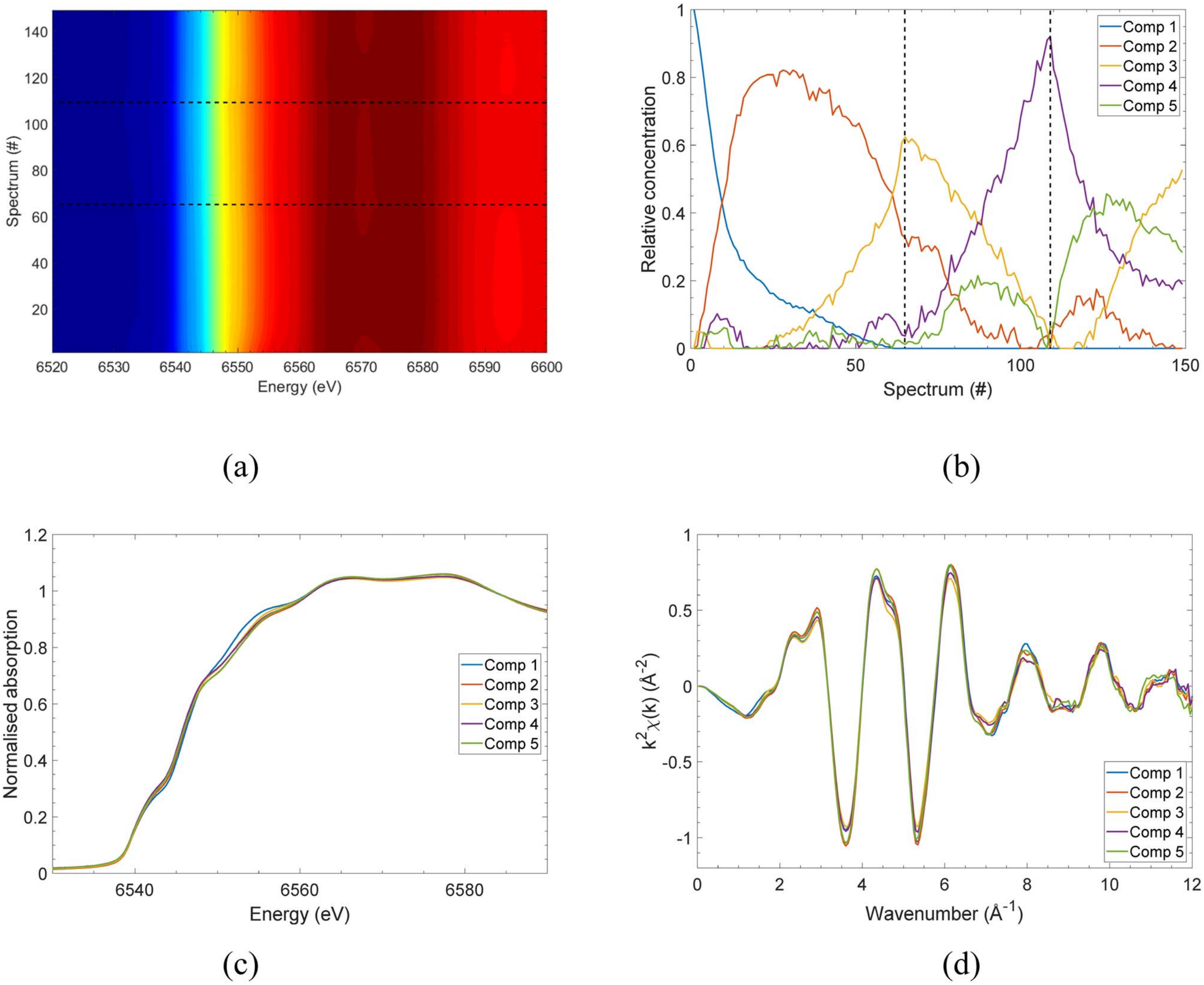

(a) (b)

(c) (d)

Fig. 8 Mn K-edge XAS spectra collected during the first 1.5 cycles in the potential range of 0.4–1.5 V for a MnP_4 electrode *vs.* Li metal, and MCR-ALS components and concentrations reconstructed from the analysis of the whole dataset: (a) topographic view of the XANES spectra; (b) relative concentrations of the MCR-ALS components; (c) XANES and (d) EXAFS portions of the MCR-ALS components.

components were eventually used in the MCR-ALS analysis, which provides "pure" spectral components expressing (by their linear combination) the main modifications in the XAS spectra (Fig. SI 14 and Table S1). The evolution of their respective relative concentration along the series of spectra is shown in Fig. 8(b), while their shape in the XANES and EXAFS region is depicted in Fig. 8(c) and (d), respectively. Very clearly, the five MCR-ALS components are very similar, with only minor but significant modifications in the edge shape, and almost no difference in the EXAFS region.

During the first discharge, the first component transforms sequentially into component 2 and then component 3, which represents the material at the end of the process. Along the following charge, the reaction goes through several intermediate states before ending with component 4, which is different from component 1. These observations indicate a minor and localized irreversible rearrangement occurring during the first lithiation, as component 1 is not fully restored upon delithiation. Importantly, these changes remain very limited in amplitude, do not involve a change in Mn oxidation state, and do not propagate upon further cycling.

Similar observations can be made for the EXAFS spectra, which are almost identical for all materials. This similarity is also reflected in their FT signals (Fig. SI 14), where only a slight change in intensity is observed in the first coordination shell. As several sub-shells contribute to these signals, only an analytical fit of the spectra can highlight differences in the local structure around the Mn centres in the different MCR-ALS components. In this case, the same model, *i.e.*, the crystal structure of MnP_4 was used to fit the five EXAFS spectra up to $R = 3.6$ (see detailed fits of the EXAFS spectra in Fig. SI 14 and Table S1). This strategy provided satisfactory fits for all components, with very minor modifications of the coordination shells, reflecting only minor structural modifications during Li (de)insertion in the MnP_4 structure. These results show that, in this potential range, in spite of a slight modification during the first discharge, possibly due to an irreversible partial amorphisation of the structure reflected in the increased Debye–Waller factors of the

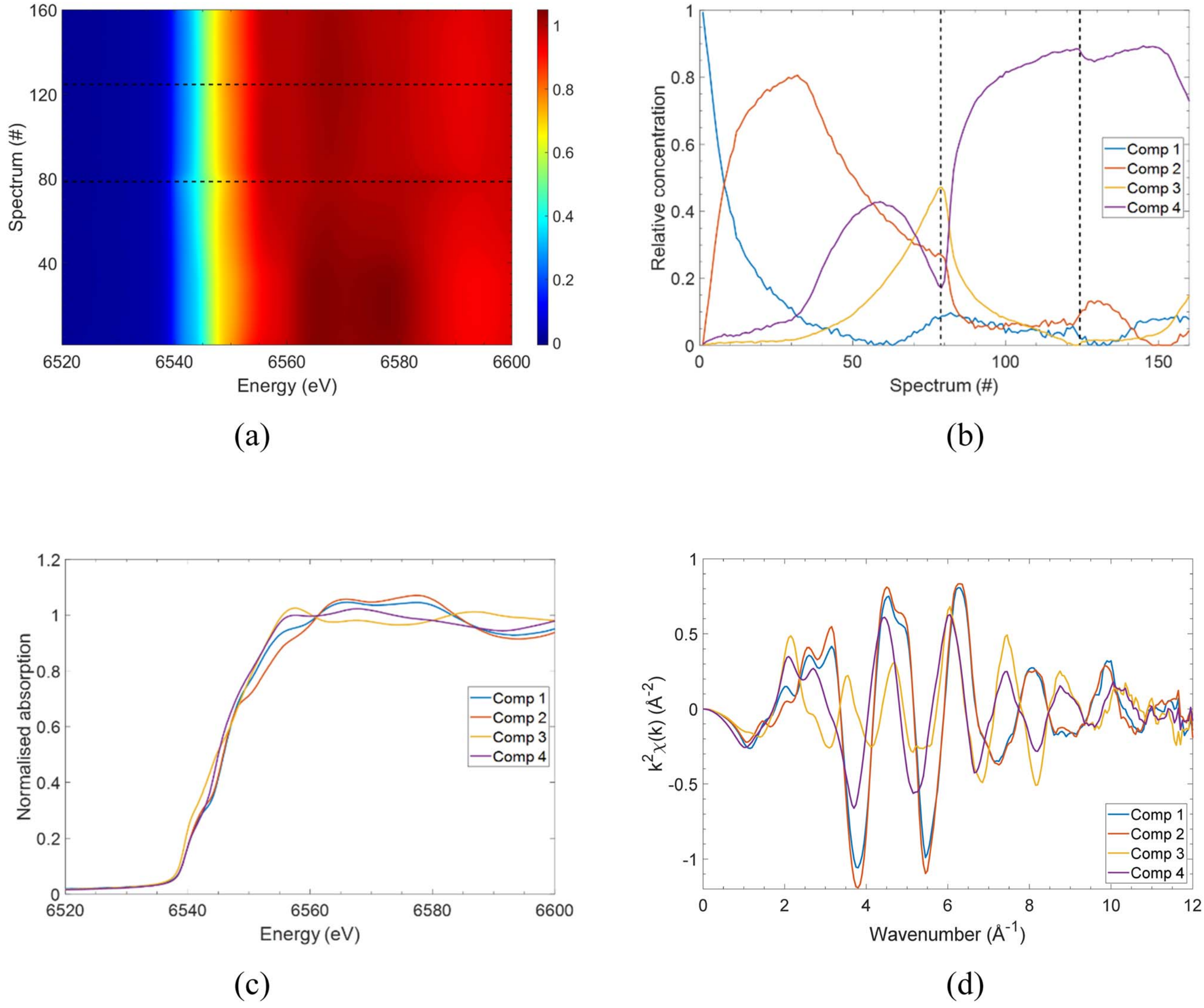

Fig. 9 Mn K-edge XAS spectra collected during the first 1.5 cycles in the potential range of 0.01–1.5 V for a MnP_4 electrode *vs.* Li metal, and MCR-ALS components and concentrations reconstructed from the analysis of the whole dataset: (a) topographic view of the XANES spectra; (b) relative concentrations of the MCR-ALS components; (c) XANES and (d) EXAFS portions of the MCR-ALS components.

P neighbours beyond the first shell, the MnP_4 structure is largely preserved.

The same strategy was then used to analyse the 161 spectra collected during the first 1.5 cycles of MnP_4 *vs.* Li with a low voltage cut-off at 0.01 V (Fig. SI 15). The results of this analysis are shown in Fig. 9. As in the previous case, the results of PCA (Fig. SI 16, SI 17, Table S2) indicate that 3 to 5 principal components are necessary to interpret the whole dataset, expressing more than 99.9% of the corresponding variance. In this case, MCR-ALS analyses were carried out with 4 or 5 "pure" spectral components, leading to very similar solutions. In fact, tests using 5 components resulted only in splitting component 4 into two subcomponents with very slightly different XANES and virtually identical EXAFS signals. For this reason, the analysis with 4 components was retained and is shown here.

The evolution of their respective relative concentration along the series of spectra is shown in Fig. 9(b), while their shape in the XANES and EXAFS region is depicted in Fig. 9(c) and (d), respectively. In contrast to cycling above 0.4 V, major changes in both XANES and EXAFS signals are detected when the voltage is further decreased. While component 1 corresponds to the pristine material and component 2 is very similar to component 3 of the previous analysis, corresponding to the material at 0.4 V, the XANES shapes of components 3 and 4 are totally different and indicate the formation of new species, in line with significant changes in the nature of the Mn species in the material at low potential. While the shape is different, the edge position of component 4, which starts forming at the beginning of the low voltage plateau below 0.4 V, is globally similar to that of components 1 and 2, suggesting that new Mn-containing phosphide species are obtained, whereas the edge of component 3, which is dominating at 0.01 V, shifts to lower energies, very close to the edge position of Mn metal.

During the following charge, component 4, corresponding to the new Mn phosphide species formed in the low voltage plateau, grows rapidly and becomes largely dominant at the end

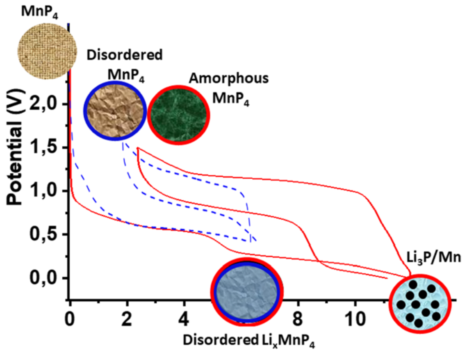

Fig. 10 Schematical view of the lithiation/delithiation mechanism of ball-milled MnP$_4$.

of the process. A partial reformation of component 3 is observed at the end of the second discharge.

The analysis of the EXAFS portions of these components (see SI 13 and Table S2 for the detailed fits of the EXAFS spectra) was necessary to gain insight into the nature of these species. The first two components (1 and 2) explain the main transformations observed during the high voltage plateau, and correspond to the irreversible decrease in the intensity of the second shell signal, indicating a slight but irreversible amorphisation of the structure of MnP$_4$, which is nevertheless globally retained. The fit of component 4, which is formed along the low voltage plateau, was carried out by assuming the formation of a Mn-rich phosphide Mn$_x$P. For this reason, fits with the local structure of several phosphide species (*e.g.*, MnP and Mn$_2$P) were attempted, and the best fit was obtained by starting from the structure of Mn$_2$P, only with a slightly lower number of Mn neighbours. For this reason, this component is attributed to amorphous Mn-rich Mn$_x$P species.

The EXAFS portion of component 3, in contrast, can be fitted by including only Mn neighbours. As only the first coordination shell is available, it is impossible to verify whether this component represents α-Mn or γ-Mn. The reduced number of nearest neighbours found with respect to either structure, however, is in line with the expected formation of Mn metal at the end of the conversion reaction. During the following charge and discharge, amorphous Mn$_x$P is reformed, and then partially transforms back, even though only partially, to Mn metal.

In summary, the EXAFS analysis indicates that the MnP$_4$ structure is preserved along the high voltage plateau, where only a Li insertion reaction is occurring, whereas conversion to Mn-rich amorphous Mn$_x$P species occurs in the low voltage plateau, eventually leading to the formation of Mn metal.

These results agree well with ^{31}P MAS NMR analysis, which indicates that Li$_3$P starts forming already at 0.4 V, along the low voltage plateau, which corresponds to the extrusion of phosphorus from MnP$_4$. The combined analyses of NMR and XAS allowed the identification of the phosphorus and manganese species formed during successive discharges and charges. From then on, it appears that the first process at 0.4 V corresponds more to an insertion of lithium without a noticeable modification of the pristine structure, which allows obtaining good reversibility and maintaining the capacity during long-term cycling as shown in Fig. 2.

On the basis of the structural and chemical transformations occurring during (de)lithiation and delithiation detected by *operando* XRD, XAS, and NMR analyses, the different cycling stabilities observed in the various potential windows can be easily rationalised. In fact, when cycling is extended to low potentials (0–0.4 V), the insertion process is followed by conversion reactions involving phosphorus extrusion and the formation of amorphous Mn-rich phosphides and Mn metal. These conversion reactions induce significant and irreversible local structural damage, leading to rapid capacity fading upon cycling.

In contrast, when the low-voltage cut-off is increased above 0.4 V, the conversion process is effectively suppressed. In this restricted potential window, MnP$_4$ undergoes predominantly lithium insertion, accompanied only by a minor first-cycle local structural accommodation. Once this stable insertion host is established, subsequent cycles proceed without further structural degradation, resulting in excellent capacity retention and a Coulombic efficiency that approaches 100%.

4 Conclusion

MnP$_4$, easily prepared from inexpensive Mn and P precursors by ball milling, represents a promising negative electrode material for LIBs. Using an optimised aqueous electrode formulation based on a CMC binder and a mixture of conductive carbon additives, a stable capacity around 600 mAh g^{-1} can be maintained for more than 60 cycles provided that cycling is restricted to an appropriate potential window. Applying a low voltage cut-off at 0.55 V suppresses the low-potential conversion reaction into Li$_3$P and Mn metal, thus limiting the capacity but significantly improving the long-term capacity retention.

The electrochemical mechanism seems to be partially different from that reported for highly crystalline MnP$_4$, where crystalline Li$_7$MnP$_4$ was observed during discharge by *ex situ* XRD at the end of the first plateau (0.5 V), followed by the reformation of MnP$_4$ upon subsequent delithiation. In the present case, as schematically represented in Fig. 10, the mechanochemically prepared MnP$_4$ is more disordered, and neither well-crystallized Li$_7$MnP$_4$ nor crystalline MnP$_4$ are obtained at mid discharge and at the end of the subsequent charge, respectively. This structural disorder appears to favour improved reversibility and electrochemical performance.

The combined *operando* XRD, Mn M-edge XAS and *ex situ* ^{7}Li and ^{31}P MAS NMR analyses allow a consistent mechanism to be proposed. Above 0.4 V, MnP$_4$ undergoes reversible lithium insertion accompanied by a slight, first-cycle local structural rearrangement, after which a stable and highly reversible insertion mechanism is established. The initial structural accommodation involves a limited and localised amorphisation detected by XAS but not by XRD, and does not affect long-term electrochemical reversibility.

In contrast, below 0.4 V, major structural changes occur: phosphorus extrusion leads to the formation of amorphous Mn-rich Mn$_x$P species, which are finally transformed into Mn metal at 0 V. These conversion reactions correlate with rapid capacity fading when the potential window is not restricted.

Future work will focus on extended full-cell cycling. A restricted potential window will then be favored for the MnP_4 electrode, where reversible lithium insertion occurs with limited structural modification, in order to limit volume changes and maximize cycling performance.

Conflicts of interest

The authors declare that they have no known competing financial interests or personal relationships that could have appeared to influence the work reported in this paper.

Data availability

The data supporting the findings of this study are available within the article and its supplementary information (SI). Additional data are available from the corresponding author upon reasonable request. Supplementary information is available. See DOI: https://doi.org/10.1039/d6ta00420b.

Acknowledgements

ANR is acknowledged for funding through the project Labex STORE-EX (Grant ANR-10-LABX-76-01). Synchrotron SOLEIL is acknowledged for providing beamtime at beamline ROCK (proposal no. 20190882). Antonella Iadecola (RS2E) is gratefully acknowledged for technical and logistic help in the preparation and the realisation of the measurement session at the synchrotron. Stéphanie Belin (Synchrotron Soleil) is acknowledged for technical help.

References

1 S. Boyanov, J. Bernardi, E. Bekaert, M. Ménétrier, M.-L. Doublet and L. Monconduit, *Chem. Mater.*, 2009, **21**, 298–308.

2 J. Fullenwarth, A. Darwiche, A. Soares, B. Donnadieu and L. Monconduit, *J. Mater. Chem. A*, 2014, **2**, 2050–2059.

3 S. Boyanov, F. Gillot and L. Monconduit, *Ionics*, 2008, **14**, 125–130.

4 Z. Li and H. Zhao, *J. Mater. Chem. A*, 2018, **6**, 24013–24030.

5 G. Chang, Y. Zhao, L. Dong, D. P. Wilkinson, L. Zhang, Q. Shao, W. Yan, X. Sun and J. Zhang, *J. Mater. Chem. A*, 2020, **8**, 4996–5048.

6 Q. Li, D. Yang, H. Chen, X. Lv, Y. Jiang, Y. Feng, X. Rui and Y. Yu, *SusMat*, 2021, **1**, 359–392.

7 S. Boyanov, D. Zitoun, M. Ménétrier, J.-C. Jumas, M. Womes and L. Monconduit, *J. Phys. Chem. C*, 2009, **113**, 21441–21452.

8 S. Ha, J. Kim, D. W. Kim, J. M. Suh and K.-H. Kim, *Batteries*, 2025, **11**, 54.

9 S. Merk, S. Kollmannsberger, S. Zeitz, V. Baran, A. Senyshyn and T. F. Fässler, *Inorg. Chem.*, 2025, **64**, 16902–16911.

10 J. Fullenwarth, B. Fraisse, N. Dupré, L. Stievano and L. Monconduit, *J. Mater. Chem. A*, 2023, **11**, 23950–23960.

11 J.-B. Leriche, S. Hamelet, J. Shu, M. Morcrette, C. Masquelier, G. Ouvrard, M. Zerrouki, P. Soudan, S. Belin, E. Elkaïm and F. Baudelet, *J. Electrochem. Soc.*, 2010, **157**, A606–A610.

12 V. Briois, C. La Fontaine, S. Belin, L. Barthe, T. Moreno, V. Pinty, A. Carcy, R. Girardot and E. Fonda, *J. Phys., Conf. Ser.*, 2016, **712**, 012149.

13 C. Ruckebusch and L. Blanchet, *Anal. Chim. Acta*, 2013, **765**, 28–36.

14 A. de Juan, J. Jaumot and R. Tauler, *Anal. Methods*, 2014, **6**, 4964.

15 A. Iadecola, A. Perea, L. Aldon, G. Aquilanti and L. Stievano, *J. Phys. D Appl. Phys.*, 2017, **50**, 144004.

16 T. Broux, T. Bamine, L. Simonelli, L. Stievano, F. Fauth, M. Ménétrier, D. Carlier, C. Masquelier and L. Croguennec, *J. Phys. Chem. C*, 2017, **121**, 4103–4111.

17 I. Landa-Medrano, A. Sorrentino, L. Stievano, I. Ruiz de Larramendi, E. Pereiro, L. Lezama, T. Rojo and D. Tonti, *Nano Energy*, 2017, **37**, 224–231.

18 B. Ravel and M. Newville, *J. Synchrotron Radiat.*, 2005, **12**, 537–541.

19 D. Massiot, F. Fayon, M. Capron, I. King, S. Le Calvé, B. Alonso, J.-O. Durand, B. Bujoli, Z. Gan and G. Hoatson, *Magn. Reson. Chem.*, 2002, **40**, 70–76.

20 F. Gillot, L. Monconduit and M.-L. Doublet, *Chem. Mater.*, 2005, **17**, 5817–5823.

21 F. Gillot, L. Monconduit, M. Morcrette, M.-L. Doublet, L. Dupont and J.-M. Tarascon, *Chem. Mater.*, 2005, **17**, 3627–3635.

22 M.-P. Bichat, F. Gillot, L. Monconduit, F. Favier, M. Morcrette, F. Lemoigno and M.-L. Doublet, *Chem. Mater.*, 2004, **16**, 1002–1013.

23 D. C. S. Souza, V. Pralong, A. J. Jacobson and L. F. Nazar, *Science*, 2002, **296**, 2012–2015.

24 A. J. Ilott, S. Chandrashekar, A. Klöckner, H. J. Chang, N. M. Trease, C. P. Grey, L. Greengard and A. Jerschow, *J. Magn. Reson.*, 2014, **245**, 143–149.

25 B. Hu, R. Yu and H. Zou, *NDT E Int.*, 2012, **47**, 66–69.

26 K. Gotoh, M. Izuka, J. Arai, Y. Okada, T. Sugiyama, K. Takeda and H. Ishida, *Carbon*, 2014, **79**, 380–387.

27 B. J. Walder, M. S. Conradi, J. J. Borchardt, L. C. Merrill, E. G. Sorte, E. J. Deichmann, T. M. Anderson, T. M. Alam and K. L. Harrison, *Sci. Adv.*, 2021, **7**(37), eabg8298.

28 M. Jouni, A. Buzlukov, M. Bardet, F. Da Cruz-Boisson, A. Eddarir, V. Massardier and G. Boiteux, *Compos. Sci. Technol.*, 2014, **104**, 104–110.

29 S. Hayes, L. Van Wüllen, H. Eckert, W. R. Even, R. W. Crocker and Z. Zhang, *Chem. Mater.*, 1997, **9**, 901–911.

30 E. Bekaert, J. Bernardi, S. Boyanov, L. Monconduit, M.-L. Doublet and M. Ménétrier, *J. Phys. Chem. C*, 2008, **112**, 20481–20490.

31 C. Marino, L. Boulet, P. Gaveau, B. Fraisse and L. Monconduit, *J. Mater. Chem.*, 2012, **22**, 22713–22720.